Evolution of charge order topology across a magnetic phase transition in cuprate superconductors

Mingu Kang[1], Jonathan Pelliciari[1], Alex Frano[2,3], Nicholas Breznay[2], Enrico Schierle[4], Eugen Weschke[4], Ronny Sutarto[5], Feizhou He[5], Padraic Shafer[6], Elke Arenholz[6], Mo Chen[2], Keto Zhang[2], Alejandro Ruiz[2], Zeyu Hao[2], Sylvia Lewin[2], James Analytis[2], Yoshiharu Krockenberger[7], Hideki Yamamoto[7], Tanmoy Das[8] and Riccardo Comin[1]*

Charge order is now accepted as an integral constituent of cuprate high-temperature superconductors, one that is intimately related to other electronic instabilities including antiferromagnetism and superconductivity[1–11]. Unlike conventional Peierls density waves, the charge correlations in cuprates have been predicted to display a rich momentum space topology depending on the underlying fermiology[12–18]. However, charge order has only been observed along the high-symmetry Cu–O bond directions. Here, using resonant soft X-ray scattering, we investigate the evolution of the full momentum space topology of charge correlations in T'-(Nd,Pr)$_2$CuO$_4$ as a function of electron doping. We report that, when the parent Mott insulator is doped, charge correlations first emerge with full rotational symmetry in momentum space, indicating glassy charge density modulation in real space possibly seeded by local defects. At higher doping levels, the orientation of charge correlations is locked to the Cu–O bond directions, restoring a more conventional long-ranged bidirectional charge order. Through charge susceptibility calculations, we reproduce the evolution in topology of charge correlations across the antiferromagnetic phase boundary and propose a revised phase diagram of T'-Ln$_2$CuO$_4$ with a superconducting region extending toward the Mott limit.

In cuprates, an unconventional momentum–space electronic structure rapidly surfaces after doping carriers into the parent Mott insulator. The unconventional fermiology of lightly doped cuprates is embodied by the 'pseudogap' regime, where coherent quasiparticle excitations are only found in a small part of the Brillouin zone[19,20]. In this emergent state, electronic carriers in the CuO$_2$ planes concomitantly organize into periodically modulated patterns in real space[1–11]. Visualization and elucidation of the microscopic link between these density waves and the many-body fermiology is a stepping stone towards understanding the nature of charge order and its relationship to Mott physics, the pseudogap and high-temperature superconductivity. In hole-doped cuprates, charge order has been mapped out to a great extent[3], yet its origin and driving mechanism remain unclear. In Bi-based compounds, scanning tunnelling microscopy (STM)[2,4,7,8] and resonant X-ray scattering (RXS)[7,8] experiments have proposed that an instability of

the pseudogapped Fermi surface might underlie the development of charge ordering. This proposal captures the temperature and doping dependence of charge order[3,7,8], and has been supported by charge susceptibility calculations in various implementations[16–18]. On the other hand, recent STM and resonant inelastic X-ray scattering studies detect charge order outside the pseudogap phase (that is, in the very underdoped or overdoped limits), leaving the exact relationship between the charge order and fermiology unsettled[21,22].

Electron-doped cuprates are an alternative platform with which to gain new perspectives on this problem, given their analogies to hole-doped cuprates in the phenomenology of charge order[10,11]. In contrast to hole-doped systems, here antiferromagnetic (AFM) correlations persist over a wide doping range (Fig. 1a) and deeply influence the many-body fermiology of electron-doped cuprates, as reflected in the appearance of an AFM pseudogap and the evolution of the Fermi surface topology with doping[20,23]. Furthermore, in these systems charge order populates a doping region characterized by strong AFM correlations[10,11], setting an ideal stage to study the interplay between the spin and charge degrees of freedom in cuprates.

The intimate relationship between AFM and charge order has been explored in numerous theoretical studies[12–15] that have focused on density wave instabilities localized along the Cu–O bond directions, in accordance with experimental reports[1–11]. At the same time, theory suggests that strong AFM correlations might induce charge instabilites in broader regions of momentum space (**Q**-space)[12,13,15]. Charting the topology of charge correlations in electron-doped cuprates is thus a new opportunity to probe the connection between charge order, antiferromagnetism and many-body fermiology in cuprates.

Here, we investigate the evolution of the momentum-space topology of charge correlations in T'-Ln$_2$CuO$_4$ (Ln = Nd, Pr) thin films as a function of electron doping. In contrast to the widely studied Ce-doped superconductors (T'-Ln$_{2-x}$Ce$_x$CuO$_4$), thin films of T'-Ln$_2$CuO$_4$ can host superconductivity without cation substitution when subjected to post-growth reduction annealing procedures[24]. The possibility of superconductivity in the 'undoped' limit questions the very Mott nature of the parent T'-cuprates, and alternative scenarios involving a Slater mechanism have been proposed[24,25].

[1]Department of Physics, Massachusetts Institute of Technology, Cambridge, MA, USA. [2]Department of Physics, University of California, Berkeley, CA, USA. [3]Department of Physics, University of California, San Diego, CA, USA. [4]Helmholtz-Zentrum Berlin für Materialien und Energie, Berlin, Germany. [5]Canadian Light Source, Saskatoon, Saskatchewan, Canada. [6]Advanced Light Source, Lawrence Berkeley National Laboratory, Berkeley, CA, USA. [7]NTT Basic Research Laboratories, NTT corporation, Atsugi, Japan. [8]Department of Physics, Indian Institute of Science, Bangalore, India. *e-mail: rcomin@mit.edu
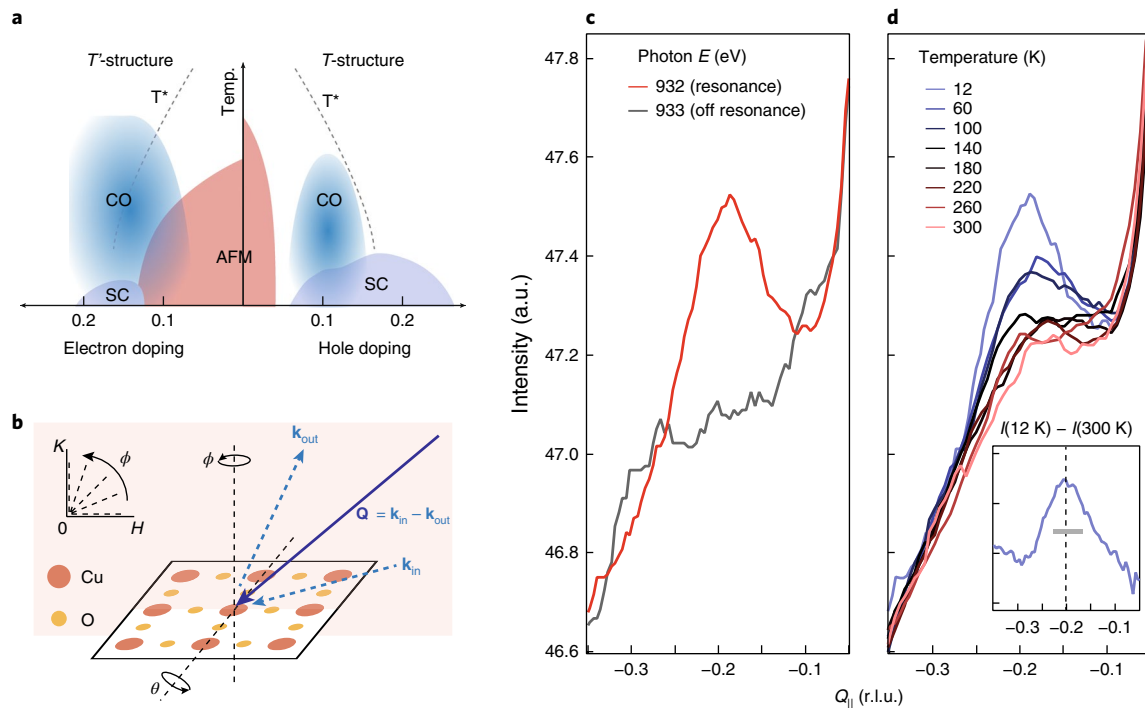
Fig. 1 | Charge correlations in T'-Nd$_2$CuO$_4$ (T'-NCO#1) along the Cu–O bond directions. a, Doping–temperature phase diagram of cuprates, with superconducting (SC), antiferromagnetic (AFM), charge ordering (CO) and pseudogap (T*) regions highlighted. **b**, Schematics of the RXS experimental geometry. Blue dashed arrows represent the wave vectors of incoming ($\mathbf{k}_{in}$) and outgoing ($\mathbf{k}_{out}$) photons, whose difference defines the total momentum transfer $\mathbf{Q}$ to the sample. Inset: the region of $\mathbf{Q}$-space that can be spanned by a combination of in-plane (θ) and out-of-plane (ϕ) rotations. **c,d**, Photon energy (**c**) and temperature (**d**) dependence of RXS scans along the Cu–O bond direction. Data in **c** (**d**) were obtained at 12 K (932 eV). Inset in **d**: the 12 K RXS scan after subtracting the room-temperature (300 K) profile. The grey line represents the half-width at half-maximum.

On the other hand, recent angle-resolved photoemission spectroscopy (ARPES), X-ray photoemission spectroscopy and X-ray absorption spectroscopy studies concluded that superconducting T'-Ln$_2$CuO$_4$ is actually electron-doped, presumably due to oxygen vacancies[26–28]. However, the exact doping–temperature phase diagram remains unclear due to difficulties in estimating the intrinsic electron concentration in these samples.

Figure 1b illustrates the schematics of our experimental set-up. In RXS experiments, the in-plane component of momentum transfer ($Q_{\parallel}$) is scanned by rotating the sample about the axis perpendicular to the scattering plane (θ). To access the full $\mathbf{Q}$-space structure of charge correlations, we acquired successive θ scans for different orientations of the CuO$_2$ planes, obtained by varying the azimuthal angle ϕ. The range of $\mathbf{Q}$-space canvassed by this method is schematically shown in the inset of Fig. 1b.

We first demonstrate the presence of enhanced charge correlations in T'-Nd$_2$CuO$_4$ (referred to as T'-NCO#1) along the Cu–O bond directions ($\phi = 0°$). Figure 1c,d presents a series of RXS scans as a function of photon energy and temperature. When the photon energy is tuned to the maximum of the Cu–L_3 absorption edge ($E \approx 932$ eV), the scattered intensity displays clear peaks in momentum space centred at $|Q_{\parallel}| \approx 0.2$ reciprocal lattice units (r.l.u.) (Fig. 1c). The scattering peak rapidly vanishes as the photon energy is tuned off resonance, confirming that it originates from electrons in the CuO$_2$ planes. As displayed in Fig. 1d, the intensity of this peak smoothly diminishes with increasing temperature, but survives up to room temperature, as in other electron-doped cuprates[10,11]. After subtracting the room-temperature background from the 12 K data (inset of Fig. 1d), we extract a correlation length of $\xi \approx 5$–6 unit cells or ~20–25 Å. Such short-ranged charge correlations have been seen in other cuprates,

(Nd,La)$_{2-x}$Ce$_x$CuO$_4$ (NCCO, LCCO), Bi$_2$Sr$_{2-x}$La$_x$CuO$_{6+\delta}$ (BSLCO) and HgBa$_2$CuO$_{4+\delta}$ (HgBCO)[8–11].

The presence of periodic charge modulations in the CuO$_2$ planes indirectly reflects the intrinsic carrier doping in the chemically undoped T'-Ln$_2$CuO$_4$ (refs. [26–28]). The observed wavevector of charge modulations (Q_c) can be used to estimate the carrier concentration from experimental measurements of Q_c versus doping in both hole- and electron-doped cuprates[3,5,8,11]. Previous RXS studies reported that Q_c in electron-doped cuprates (NCCO, LCCO) increases with higher electron content, similarly to hole-doped cuprates (BSLCO, HgBCO and YBCO). From previous estimates[10,11], the observed wavevector of T'-NCO#1 ($Q_c \approx 0.2$ r.l.u.) maps onto an electron density of $n \approx 0.07 \pm 0.02$ per Cu, placing our sample at the low-doping limit of the phase diagram. This assignment of doping level is consistent with temperature-dependent Hall measurements performed on the same T'-Ln$_2$CuO$_4$ films (see Supplementary Information).

In this low-doping limit, we successively performed RXS scans at various azimuthal angles ϕ to map the complete $\mathbf{Q}$-space topology of charge correlations. Surprisingly, as shown in Fig. 2a, broad but clear diffraction peaks are detected along all investigated momentum directions ($\phi = 0$, 15, 30, 45, 65 and 90°; see Supplementary Figs. 1 and 2 for the full data sets). To investigate this feature in more detail, we subtracted a slowly varying fluorescence background from each scan and plotted the residual resonant peaks (Fig. 2b). The peaks display almost identical intensity, wavevector ($Q_c \approx 0.2 \pm 0.02$ r.l.u.) and linewidth (half-width at half-maximum of ~0.07 ± 0.02 r.l.u.), regardless of the probed momentum direction. Furthermore, the detailed temperature and photon-energy dependence of the scattering peaks at representative azimuthal angles (0, 15 and 45°, Fig. 2g,h) fall into a single curve within experimental errors, indicating these structures arise from the same state. The two-dimensional plot in
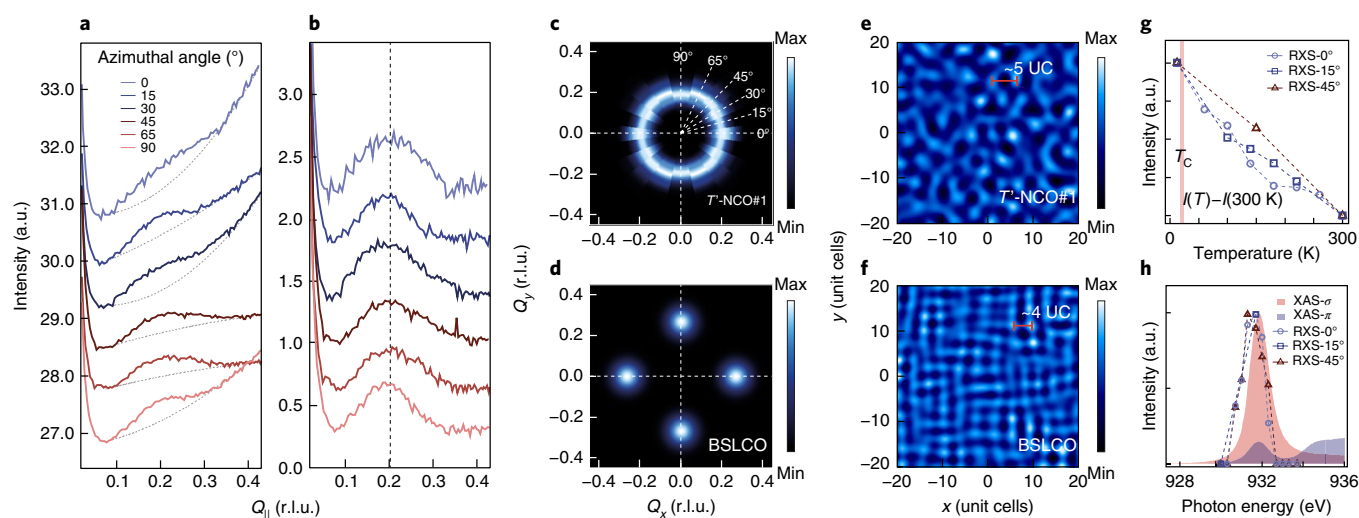
Fig. 2 | Full momentum–space topology of charge correlations in T'-NCO#1. a, RXS scans of T'-NCO#1 for various azimuthal angles. Curves are shifted vertically for clarity. Overlaid grey dotted lines represent polynomial fits to the fluorescence backgrounds. **b**, Charge correlation peaks derived from **a** after background subtraction. **c,d**, Momentum space topology of charge correlations (structure factor) in T'-NCO#1 (**c**) and BSLCO (**d**): polar plots of data from **b** (**c**) and from data in ref. [8] (**d**). **e,f**, Simulated real-space charge density modulations $\delta\rho(\mathbf{r})$ corresponding to the structure factors in **c** and **d**, respectively. UC, unit cells. **g,h**, Temperature (**g**) and photon energy (**h**) dependence of RXS intensities at representative azimuthal angles 0, 15 and 45°. Shaded profiles in **h** represent the Cu–L_3 edge X-ray absorption scans with σ/π incoming polarizations.

Fig. 2c summarizes this observation, highlighting the fact that, at low doping levels, the charge correlations in the CuO_2 plane possess full (C_{inf}) rotational symmetry in **Q**-space. This result is in marked contrast to all previous reports of bond-oriented charge order in cuprates (Fig. 2d)[3,5–11], and demonstrates that, on electron doping to the parent Mott/Slater insulator, charge correlations initially develop a complex **Q**-space structure that was entirely unanticipated. To rule out an extrinsic origin to the observed structure factor, the single crystallinity (or C_4 symmetry) of the sample was confirmed before and after the RXS experiments (Supplementary Fig. 3). Therefore, the charge correlations in T'-NCO#1 manifest a higher rotational symmetry than the underlying lattice.

To gain additional insights into the observed topology of structure factor $S(\mathbf{Q})$, we simulated a possible charge density map $\delta\rho(\mathbf{r})$. In doing so, we adopted randomly assigned reciprocal space complex phases, and thus $\delta\rho(\mathbf{r})$ represents only one of the possible realizations corresponding to $S(\mathbf{Q})$ (see Methods). The simulated map of $\delta\rho(\mathbf{r})$ in Fig. 2e depicts a 'glassy' state with an apparent tendency to periodic ordering at wavevector Q_c (with a period of five unit cells), but without any preference in orientation. This is again in sharp contrast to the case of bond-oriented charge order, whose simulated $\delta\rho(\mathbf{r})$ is shown in Fig. 2f (see also Supplementary Fig. 4).

To elucidate this new phenomenology, we recall that, within Lindhard theory[29], the linearized charge density perturbation $\rho(\mathbf{Q})$ induced by an external potential $\phi(\mathbf{Q})$ is obtained as $\rho(\mathbf{Q}) = \chi(\mathbf{Q}) \cdot \phi(\mathbf{Q})$, where the generalized charge susceptibility $\chi(\mathbf{Q})$ is directly linked to the underlying electronic band structure. In this framework, a local potential can induce Friedel oscillations of charge density (akin to quasiparticle interference modulations observed in STM), to which RXS is sensitive, as revealed by recent theoretical studies[17,30,31]. Given that the experimental observable, structure factor $S(\mathbf{Q})$, is proportional to the squared amplitude of the charge density (so that $S(\mathbf{Q}) \propto |\rho(\mathbf{Q})|^2 = |\chi(\mathbf{Q}) \cdot \phi(\mathbf{Q})|^2$), this formulation of the scattering process allows us to analyse the RXS information not only in terms of genuine long-range ordering with spontaneous symmetry breaking, but also as a direct reflection of generic many-body instabilities in the Fermi surface, encoded in the interacting charge susceptibility.

To articulate this scenario, in Fig. 3 we compare the Fermi surface topology, the **Q**-space maps of the static charge susceptibility and the **Q**-space topology of observed RXS peaks. Figure 3a–e and 3f–j, respectively, show the calculated Fermi surfaces and static charge susceptibilities of T'-NCO at various representative doping levels. The calculation is based on the momentum-resolved density fluctuation model, which has been used to capture certain experimental characteristics of charge order in hole-doped cuprates from instabilites in the Fermi surface (see Methods for details)[18]. In electron-doped systems, the longitudinal spin and charge susceptibilities become mixed in the presence of commensurate AFM correlation[32], which results in the spin–charge interaction being distinct from the incommensurate stripe physics of hole-doped cuprates (see Supplementary Information for details). In the low-doping limit ($n = 0.05$, Fig. 3a) with strong AFM correlations, the electrons first fill the upper Hubbard states at the antinodes, developing electron pockets around $(\pm\pi, 0)/(0, \pm\pi)$ that are very circular in this limit due to the presence of strong $(\pm\pi, \pm\pi)$ AFM scattering. Correspondingly, the interacting charge susceptibility is enhanced uniformly along all azimuthal directions at $|Q_{\|}| = 0.2$ r.l.u. (Fig. 3f,l), in remarkable accordance with the observed **Q**-space structure of the scattering peaks in T'-NCO#1 (Fig. 3k,m). This analysis demonstrates that the RXS structures in Fig. 2 reflect the rotationally symmetric particle–hole scattering channels connecting low-energy states across the Fermi surface, which materialize in real space possibly through the defect- or impurity-induced Friedel oscillations in charge density[17,30,31]. We note that oxygen vacancies, a likely source of doping in T'-Ln_2CuO_4, might provide the pinning potential $\phi(\mathbf{Q})$ in this framework.

The dramatic change in Fermi surface topology occurs near the AFM critical point, where the termination of Néel order accompanies the collapse of the Mott gap, resulting in the formation of hole pockets at $(\pm\pi/2, \pm\pi/2)$ (Fig. 3c,d). With the weakening of (π,π) AFM scattering, the charge susceptibility becomes anisotropic, and is enhanced around the high-symmetry Cu–O bond directions (Fig. 3h,i), recovering the C_4 symmetry of the underlying lattice. This trend continues up to the paramagnetic limit ($n = 0.17$, Fig. 3e), where the electron and hole pockets merge to form a single large
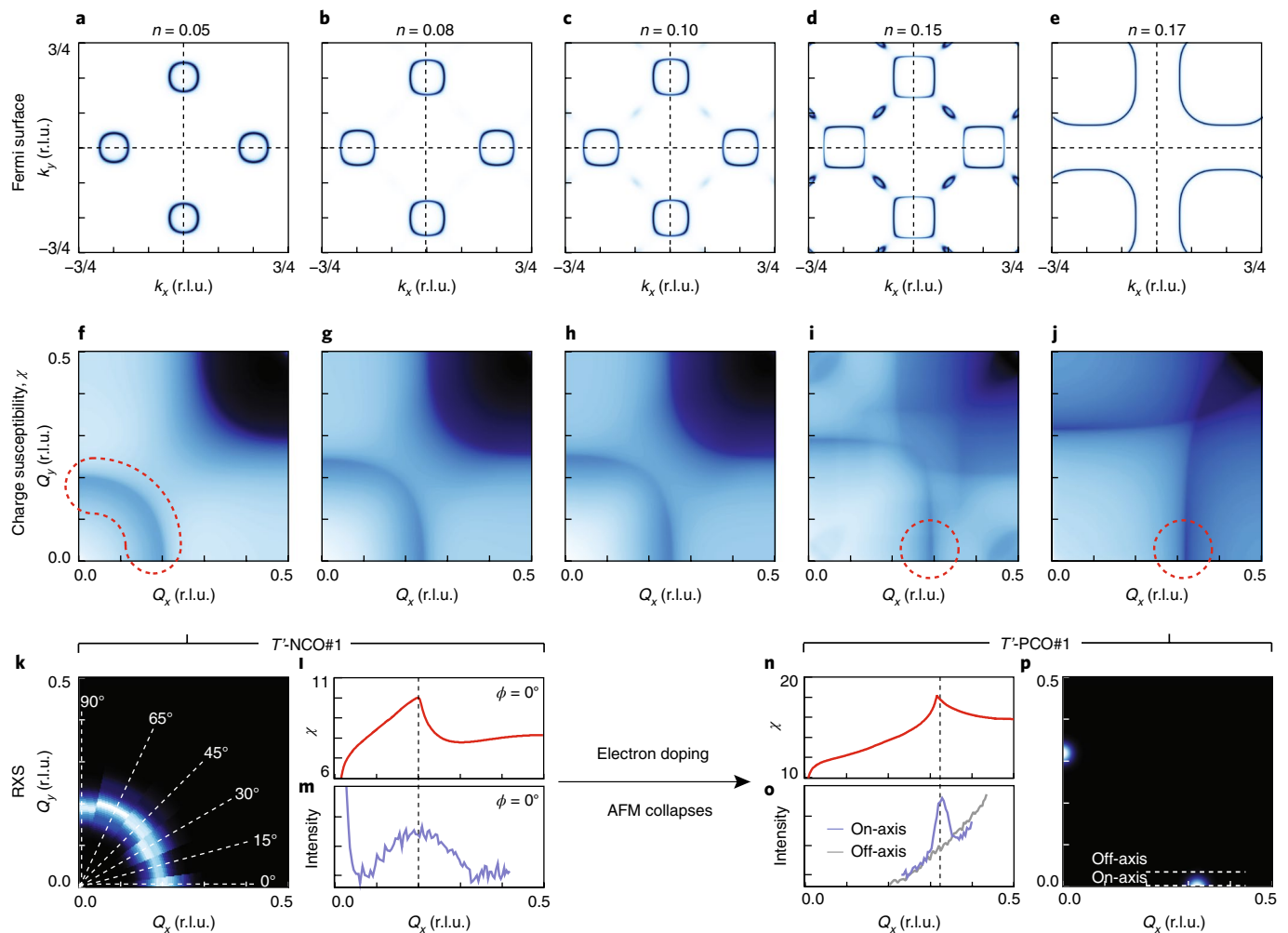
Fig. 3 | Crossover from C_{inf} to C_4 symmetric charge correlation in electron-doped cuprates. a–e, Evolution of the Fermi surface of electron-doped cuprates as a function of intrinsic electron density. **f–j**, Corresponding **Q**-space plots of the static charge susceptibilities obtained from momentum-resolved density fluctuation calculations. Red dotted lines highlight the contours where an enhanced charge response is expected. **k,p**, **Q**-space representation of charge correlations in the low-doping (T'-NCO#1, $n \approx 0.05$; **k**) and high-doping (T'-PCO#1, $n \approx 0.17$; **p**) limit. **l–o**, Comparison of charge susceptibilities (**l,n**) and RXS intensities (**m,o**) along Q_x directions at $n \approx 0.05$ (**l,m**) and $n \approx 0.17$ (**n,o**). Dotted lines in **p** represent the momentum–space segments along which the RXS profiles of T'-PCO#1 in **o** are sampled.

Fermi surface centred at $(\pm\pi, \pm\pi)$. We note that the doping evolution of the Fermi surface presented here is in close agreement with experimental Fermi surfaces obtained from ARPES and quantum oscillation experiments on electron-doped cuprates[20,23]. These calculations thus suggest that AFM order in electron-doped cuprates promotes charge correlations in all momentum directions in the low-doping limit, as detected by the present RXS experiments, while a more conventional bidirectional charge order emerges as AFM order is removed at larger doping.

To confirm the crossover from C_{inf} to C_4 topology of the charge correlation, we performed RXS measurements on the T'-Pr_2CuO_4 (T'-PCO#1) sample with higher intrinsic doping. As displayed in Fig. 3o, we observed a sharp RXS peak at $|Q_{||}| = 0.32 \pm 0.02$ r.l.u. along the Cu–O bond direction (see Supplementary Fig. 5 for details of RXS experiments on T'-PCO#1). From the empirical doping dependence of Q_c—or equivalently by comparing Q_c to the maximum wavevector of the calculated charge susceptibility (Fig. 3n) —the value $Q_c = 0.32 \pm 0.02$ r.l.u. maps to an electron density $n \approx 0.17 \pm 0.02$ (ref. [11]; see also Supplementary Information for the corresponding Hall measurements). This observation confirms

that low-doping charge correlations with C_{inf} rotational symmetry morph into a disconnected topology with charge order peaks pinned to the Cu–O bond directions in the high-doping limit, forming a more conventional type of bidirectional charge order as schematically displayed in Fig. 3p.

It is worth noting that the charge order in the high-doping limit (T'-PCO#1) is rather long-range, with a correlation length of $\xi \approx 20$ unit cells or ~80 Å, which is about four times larger than the low-doping limit (T'-NCO#1). This pronounced enhancement in spatial coherence is consistent with proposals that the charge order correlation length is affected by the degree of directionality in the underlying electronic susceptibility[17]. We note that the long correlation length of T'-PCO#1 is comparable to that in $YBa_2Cu_3O_{6+\delta}$ (YBCO), where charge order directly competes with superconductivity[5]. On the other hand, the short correlation length of T'-NCO#1 is akin to that of BSLCO and HgBCO (refs. [8,9]), where the direct competition between charge order and superconductivity is not fully established. This fact hints at a possible crossover in the nature of charge order as a function of electron doping: from an incipient ordering phenomenon in the low-doping regime, to a long-range-ordered ground state
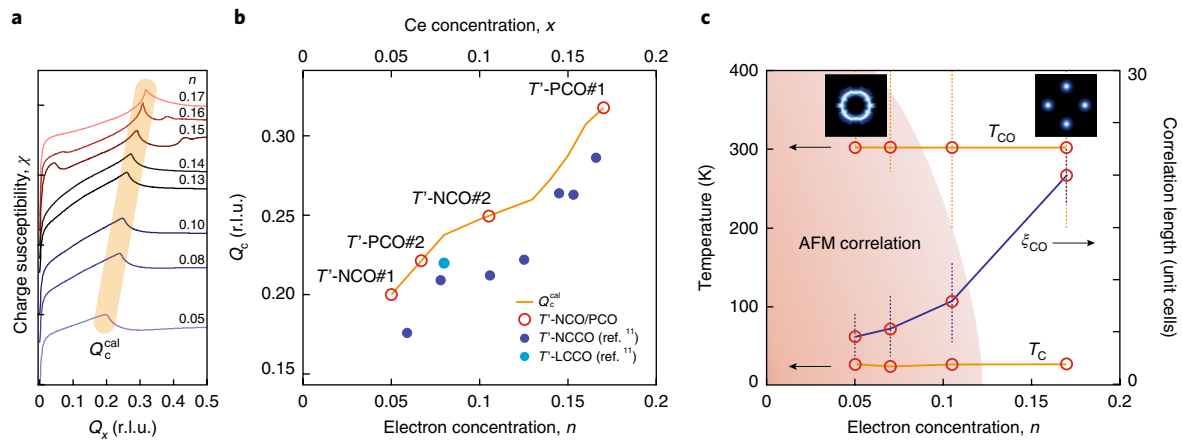
Fig. 4 | Phase diagram of T'-Ln$_2$CuO$_4$. a, Stack of charge susceptibility χ along the reciprocal Q_x axis calculated at various electron concentration n. χ displays a clear maximum at the wavevector Q_c^{cal}, which systematically increases with doping. **b**, Relationship between Q_c and dopant concentration n in electron-doped cuprates. The orange solid line tracks Q_c^{cal} versus n. Dark (light) blue dots represent the Ce-concentration dependence of Q_c in NCCO (LCCO)[11]. The four T'-Ln$_2$CuO$_4$ samples investigated here are marked by red circles. **c**, Temperature–doping phase diagram of T'-Ln$_2$CuO$_4$ with onset temperature of charge correlations (T_{CO}), superconducting transition temperature (T_c) and AFM region indicated. The latter is sketched on the basis of both neutron scattering[34] and ARPES studies[33]. Orange dotted lines represent error bars on T_{CO}, which arise from the noise level of the RXS intensity or the highest temperature investigated. Insets: momentum space topology of charge correlations in the low and high doping limits. The evolution of ξ_{CO} as a function of electron density is also overlaid as a blue solid line. Error bars for ξ_{CO} arise from inaccuracy in Gaussian fitting of the RXS peaks.

at higher electron doping as the electronic susceptibility acquires strong directionality. At the same time, the analogy between T'-NCO#1 and BSLCO and HgBCO raises an important question on the nature of charge order in these hole-doped systems: whether it is a bona fide symmetry-broken phase or rather an incipient state possibly initiated by quasiparticle scattering across the Fermi surface as observed here. Altogether, our results, combined with previous reports on hole-doped cuprates[3,5–9], hint at a common link between the low-energy fermiology and the spatial organization of the electronic state in hole- and electron-doped cuprates.

The established connection paves the way to use Q_c as a measure of intrinsic electron density. This inference is especially valuable for all T'-structured cuprates, whose unknown oxygen stoichiometry usually hinders the exact determination of their true electron density[24,26–28,33]. In Fig. 4b we plot the calculated doping dependence of Q_c as extracted from the maximum of the charge susceptibility (Fig. 4a). For comparison, we also plot the Ce-doping dependence of Q_c from previous studies of NCCO and LCCO[11]. A common trend is apparent; nonetheless, the NCCO data appear to be slightly offset to higher doping levels. To some degree, this deviation is natural because the Ce concentration cannot represent the sole factor determining carrier density in electron-doped cuprates, as emphasized in recent photoemission studies[26–28,33]. This consideration further underscores the importance of the explicit determination of intrinsic electron concentrations in T'-cuprates.

In addition to T'-NCO#1 ($Q_c \approx 0.2$ r.l.u.) and T'-PCO#1 ($Q_c \approx 0.32$ r.l.u.), as presented above, we measured two additional samples with RXS peaks at $Q_c \approx 0.22$ r.l.u. (T'-PCO#2) and $Q_c \approx 0.25$ r.l.u. (T'-NCO#2) (Supplementary Fig. 6). Based on the relationship between Q_c and n, we infer that our samples cover a wide doping range from $n \approx 0.05$ to 0.17, as shown in Fig. 4b. Interestingly, all our samples were subjected to the post-growth annealing and show superconductivity with $T_c = 24.4$, 23.1, 24.6 and 24.8 K (for T'-NCO#1, T'-PCO#2, T'-NCO#2 and T'-PCO#1, respectively), as shown in Fig. 4c. This finding reflects a persistence of the superconducting phase into the low-doping region, in contrast to the conventional phase diagram of electron-doped cuprates (Fig. 1a). This conclusion lends support to the very recent ARPES studies on bulk T'-Pr$_{2-x}$LaCe$_x$CuO$_{4-\delta}$, which also report a revised

phase diagram with an extended superconducting dome based on the intrinsic electron density estimated from Luttinger's theorem[33]. Our experimental observations challenge the conventional understanding of charge order and the phase diagram of electron-doped cuprates, and provide insights into a unified description of charge order phenomenology.

Online content

Any methods, additional references, Nature Research reporting summaries, source data, statements of data availability and associated accession codes are available at https://doi.org/10.1038/s41567-018-0401-8.

References

1. Birgeneau, R. J. et al. Static and dynamic spin fluctuations in superconducting La$_{2-x}$Sr$_x$CuO$_4$. *Phys. Rev. B* **39**, 2868–2871 (1989).
2. Hoffman, J. E. A four unit cell periodic pattern of quasi-particle states surrounding vortex cores in Bi$_2$Sr$_2$CaCu$_2$O$_{8+x}$. *Science* **295**, 466–469 (2002).
3. Comin, R. Resonant X-ray scattering studies of charge order in cuprates. *Annu. Rev. Condens. Matter Phys.* **7**, 369–405 (2016).
4. Vershinin, M. et al. Local ordering in the pseudogap state of the high-T_c superconductor Bi$_2$Sr$_2$CaCu$_2$O$_{8+\delta}$. *Science* **303**, 1995–1998 (2004).
5. Ghiringhelli, G. et al. Long-range incommensurate charge fluctuations in (Y,Nd)Ba$_2$Cu$_3$O$_{6+x}$. *Science* **337**, 821–825 (2012).
6. Chang, J. et al. Direct observation of competition between superconductivity and charge density wave order in YBa$_2$Cu$_3$O$_{6.67}$. *Nat. Phys.* **8**, 871–876 (2012).
7. da Silva Neto, E. H. et al. Ubiquitous interplay between charge ordering and high temperature superconductivity in cuprates. *Science* **343**, 393–396 (2014).
8. Comin, R. et al. Charge order driven by fermi-arc instability in Bi$_2$Sr$_{2-x}$La$_x$Cu O$_{6+\delta}$. *Science* **343**, 390–392 (2014).
9. Tabis, W. et al. Charge order and its connection with Fermi-liquid charge transport in a pristine high-T_c cuprate. *Nat. Commun.* **5**, 5875 (2014).
10. da silva Neto, E. H. et al. Charge ordering in electron doped superconductor Nd$_{2-x}$Ce$_x$CuO$_4$. *Science* **347**, 282–285 (2015).
11. da Silva Neto, E. H. et al. Doping dependent charge order correlations in electron-doped cuprates. *Sci. Adv.* **2**, e1600782 (2016).
12. Sachdev, S. & La Placa, R. Bond order in two-dimensional metals with antiferromagnetic exchange interactions. *Phys. Rev. Lett.* **111**, 027202 (2013).
13. Sau, J. D. & Sachdev, S. Mean-field theory of competing orders in metals with antiferromagnetic exchange interactions. *Phys. Rev. B* **89**, 075129 (2014).

14. Wang, Y. & Chubukov, A. Charge-density-wave order with momentum (2Q,0) and (0,2Q) within the spin-fermion model: continuous and discrete symmetry breaking, preemptive composite order, and relation to pseudogap in hole-doped cuprates. *Phys. Rev. B* **90**, 35149 (2014).

15. Wang, X., Wang, Y., Schattner, Y., Berg, E. & Fernandes, R. M. Fragility of charge order near an antiferromagnetic quantum critical point. *Phys. Rev. Lett.* **120**, 247002 (2017).

16. Atkinson, W. A., Kampf, A. P. & Bulut, S. Charge order in the pseudogap phase of cuprate superconductors. *New J. Phys.* **17**, 013025 (2015).

17. Dalla Torre, E. G., He, Y., Benjamin, D. & Demler, E. Exploring quasiparticles in high-T_c cuprates through photoemission, tunneling, and X-ray scattering experiments. *New J. Phys.* **17**, 22001 (2015).

18. Duong, L. Q. & Das, T. Correlation between Fermi arc and charge order resulting from the momentum-dependent self-energy correction in cuprates. *Phys. Rev. B* **96**, 125154 (2017).

19. Marshall, D. S. et al. Unconventional electronic structure evolution with hole doping in $Bi_2Sr_2CaCu_2O_{8+\delta}$: angle-resolved photoemission results. *Phys. Rev. Lett.* **76**, 4841 (1996).

20. Armitage, N. P. et al. Doping dependence of an n-type cuprate superconductor investigated by angle-resolved photoemission spectroscopy. *Phys. Rev. Lett.* **88**, 257001 (2002).

21. Cai, P. et al. Visualizing the evolution from the Mott insulator to a charge ordered insulator in lightly doped cuprates. *Nat. Phys.* **12**, 1047–1051 (2015).

22. Peng, Y. Y. et al. Re-entrant charge order in overdoped $(Bi,Pb)_{2.12}Sr_{1.88}CuO_{6+\delta}$ outside the pseudogap regime. *Nat. Mater.* **17**, 697–702 (2018).

23. Helm, T. et al. Evolution of the Fermi surface of the electron-doped high-temperature superconductor $Nd_{2-x}Ce_xCuO_4$ revealed by Shubnikov–de Haas oscillations. *Phys. Rev. Lett.* **103**, 157002 (2009).

24. Naito, M., Krockenberger, Y., Ikeda, A. & Yamamoto, H. Reassessment of the electronic state, magnetism, and superconductivity in high-T_c cuprates with the Nd_2CuO_4 structure. *Physica C* **523**, 28–54 (2016).

25. Weber, C., Haule, K. & Kotliar, G. Strength of correlations in electron- and hole-doped cuprates. *Nat. Phys.* **6**, 574–578 (2010).

26. Wei, H. I. et al. Electron doping of the parent cuprate La_2CuO_4 without cation substitution. *Phys. Rev. Lett.* **117**, 147002 (2016).

27. Horio, M. et al. Electronic structure of Ce-doped and -undoped Nd_2CuO_4 superconducting thin films studied by hard X-ray photoemission and soft X-ray absorption spectroscopy. *Phys. Rev. Lett.* **120**, 257001 (2018).

28. Horio, M. et al. Angle-resolved photoemission spectroscopy of the low-energy electronic structure of superconducting Pr_2CuO_4 driven by oxygen nonstoichiometry. *Phys. Rev. B* **98**, 020505 (2018).

29. Lindhard, J. On the properties of a gas of charged particles. *Kgl. Danske Videnskab. Selskab Mat.-fys. Medd.* **28**, 1–57 (1954).

30. Abbamonte, P., Demler, E., Seamus Davis, J. C. & Campuzano, J. C. Resonant soft X-ray scattering, stripe order, and the electron spectral function in cuprates. *Physica C* **481**, 15–22 (2012).

31. Dalla Torre, E. G., Benjamin, D., He, Y., Dentelski, D. & Demler, E. Friedel oscillations as a probe of fermionic quasiparticles. *Phys. Rev. B* **93**, 205117 (2016).

32. Das, T., Markiewicz, R. S. & Bansil, A. Intermediate coupling model of the cuprates. *Adv. Phys.* **63**, 151–266 (2014).

33. Song, D. et al. Electron number-based phase diagram of $Pr_{1-x}LaCe_xCuO_{4-\delta}$ and possible absence of disparity between electron- and hole-doped cuprate phase diagrams. *Phys. Rev. Lett.* **118**, 137001 (2017).

34. Motoyama, E. M. et al. Spin correlations in the electron-doped high-transition-temperature superconductor $Nd_{2-x}Ce_xCuO_{4\pm\delta}$. *Nature* **445**, 186–189 (2007).

Author contributions

M.K., J.P., E.S., A.F. and N.B. conducted the RXS experiments and analysed the data with help from M.C., K.Z., A.R., Z.H., S.L. and J.A. E.W., R.S., F.H., P.S. and E.A. maintained the X-ray beamlines and supported RXS experiments. T.D. performed the calculations. Y.K. and H.Y. grew the thin films, performed the transport measurements and analysed the data. R.C. conceived the experiment and directed the project. M.K. and R.C. wrote the manuscript with input from all other co-authors.

Competing interests

The authors declare no competing interests.

Additional information

Methods

Sample growth and characterizations. The thin films of T'-NCO and T'-PCO used in this work were grown by molecular beam epitaxy under ultrahigh vacuum using Nd, Pr and Cu metal sources and atomic oxygen generated in situ from a radiofrequency oxygen source[35]. Reflection high energy electron diffraction and electron impact emission spectroscopy were used to monitor and control the growth of the NCO and PCO films on (001) SrTiO₃ substrates in real time. High-resolution reciprocal space mapping data show that films with a thickness of 100 nm are grown fully relaxed. The films were subjected to a two-step annealing process[36]. The superconducting transition was measured by electrical transport and magnetometry.

RXS experiments. RXS experiments were performed at the UE46_PGM-1 beamline of BESSY II (T'-NCO#1, T'-NCO#2), the REIXS beamline of the Canadian Light Source (T'-PCO#1), and Beamline 4.0.2 of the Advanced Light Source (T'-PCO#2). Experiments were conducted at 12 K (unless specified) and under high vacuum (better than 10^{-9} torr). Samples were oriented in situ using Bragg reflections. All measurements were conducted at the Cu–L_3 absorption edge with out-of-scattering-plane (σ) incoming polarization to maximize the sensitivity to charge scattering. Momentum–space scans were obtained by rocking the sample angle at a fixed detector position. The temperature dependence series was acquired by both heating and cooling the samples, yielding consistent results.

Simulations of the real space charge fluctuations. The structure factor $S(\mathbf{Q})$ for T'-NCO#1 is modelled by $S(\mathbf{Q}) = \exp\left(\frac{4\ln 2(|\mathbf{Q}| - Q_c)^2}{w^2}\right)$, where the Q_c is the wavevector centroid of charge correlations, and w is the full-width at half-maximum. $S(\mathbf{Q})$ for BSLCO is similarly modelled by a 2D Gaussian function centred at $(\pm Q_c, 0)$, $(0, \pm Q_c)$. The real space charge–charge correlation function $C(\mathbf{r})$ is obtained by a discrete 2D Fourier transform of $S(\mathbf{Q})$. To simulate the real space charge density fluctuation $\delta\rho(\mathbf{r})$, we first introduce a matrix of random reciprocal-space phases $\phi(\mathbf{Q_m})$ and subsequently simulate the charge fluctuation as $\delta\rho(\mathbf{r}) = \sum_m \sqrt{S(\mathbf{Q_m})} \cos(\mathbf{Q_m} \cdot \mathbf{r} + (\mathbf{Q_m}))$, where m labels the discretized Fourier components[37].

Momentum-resolved density fluctuation calculations. We take an effective Hamiltonian near the AFM saddle point

$$H = \sum_{k,\sigma} [\xi_k c_{k,\sigma}^\dagger c_{k,\sigma} + Um\sigma c_{k+Q,\sigma}^\dagger c_{k,\sigma}] + \text{h.c.}$$

where the non-interacting dispersion ξ_k is taken from tight-binding calculation of previous works, U is the on-site Hubbard interaction, and m represents the staggered magnetization[32]. In the commensurate AFM state with $Q = (\pi, \pi)$, the longitudinal spin and charge susceptibilities become mixed in the Umklapp scattering channels, while the transverse spin susceptibilities remain decoupled. Based on the above Hamiltonian, we compute the correlation functions with many-body corrections implemented within the random-phase approximations and self-energy corrections. In the framework of the momentum-resolved density fluctuation model, both the single-particle Green's function and the two-body correlation functions are calculated self-consistently with the self-energy corrections. We included Bethe–Salpeter-type vertex corrections obeying Ward's identity. The AFM gap and chemical potential are also computed self-consistently for each doping with a doping dependent U adopted from previous studies[32]. See Supplementary Information for a detailed description of the calculation method.

Data availability

The data that support the plots within this paper and other findings of this study are available from the corresponding author upon reasonable request.

References

35. Krockenberger, Y. et al. Emerging superconductivity hidden beneath charge-transfer insulators. *Sci. Rep.* **3**, 2235 (2013).
36. Krockenberger, Y., Yamamoto, H., Tsukada, A., Mitsuhashi, M. & Naito, M. Unconventional transport and superconducting properties in electron-doped cuprates. *Phys. Rev. B* **85**, 184502 (2012).
37. Fine, B. V. Comment on 'Broken translational and rotational symmetry via charge stripe order in underdoped YBa₂Cu₃O₆₊ᵧ'. *Science* **351**, 235 (2016).